

---

# Lightweight Transformer via Unrolling of Mixed Graph Algorithms for Traffic Forecast

---

Ji Qi<sup>1</sup> Tam Thuc Do<sup>2</sup> Mingxiao Liu<sup>1</sup> Zhuoshi Pan<sup>1</sup> Yuzhe Li<sup>1</sup>  
Gene Cheung<sup>2</sup> H. Vicky Zhao<sup>1</sup>

<sup>1</sup> Department of Automation, Tsinghua University, Beijing, China

<sup>2</sup> Department of EECS, York University, Toronto, Canada

{qij21, mx-liu21, pzs23, yz-li24}@mails.tsinghua.edu.cn,  
vzhao@tsinghua.edu.cn, {dtamthuc, genec}@yorku.ca

## Abstract

To forecast traffic with both spatial and temporal dimensions, we unroll a mixed-graph-based optimization algorithm into a lightweight and interpretable transformer-like neural net. Specifically, we construct two graphs: an undirected graph  $\mathcal{G}^u$  capturing spatial correlations across geography, and a directed graph  $\mathcal{G}^d$  capturing sequential relationships over time. We formulate a prediction problem for the future samples of signal  $\mathbf{x}$ , assuming it is “smooth” with respect to both  $\mathcal{G}^u$  and  $\mathcal{G}^d$ , where we design new  $\ell_2$  and  $\ell_1$ -norm variational terms to quantify and promote signal smoothness (low-frequency reconstruction) on a directed graph. We construct an iterative algorithm based on alternating direction method of multipliers (ADMM), and unroll it into a feed-forward network for data-driven parameter learning. We insert graph learning modules for  $\mathcal{G}^u$  and  $\mathcal{G}^d$ , which are akin to the self-attention mechanism in classical transformers. Experiments show that our unrolled networks achieve competitive traffic forecast performance as state-of-the-art prediction schemes, while reducing parameter counts drastically. Our code is available in <https://github.com/SingularityUndefined/Unrolling-GSP-STForecast>.

## 1 Introduction

We study the problem of forecasting city traffic with spatial and temporal dimensions, *e.g.*, predicting car density at a set of intersections 5 minutes into the future given measurements in the past. Optimizing prediction here means exploiting both *spatial correlations* across geography and *sequential relationships* in time of how the past measurements inform future observations. When modeling the pairwise relationships as a graph, the problem is also called *time-vertex signal processing* (TVSP) [1].

Among model-based methods, one approach to TVSP is to filter the signal along the spatial and temporal dimensions independently [2]—*e.g.*, employ graph spectral filters in the *graph signal processing* (GSP) literature [3, 4] along the irregular spatial dimension, and traditional Fourier filters along the regular time dimension. Another approach is to model the spatial correlations across time as a sequence of slowly time-varying graphs, and then process each spatial signal at time  $t$  separately, where the graph changes over time are constrained by the Frobenius norm [5],  $\ell_1$ -norm [6], or low-rankness [7] of consecutive adjacency matrices. However, neither approach exploits spatial and temporal relations simultaneously for optimal performance.

Leveraging the prowess of modern *deep learning* (DL) models like transformers [8], recent data-driven efforts address TVSP by building elaborate transformer architectures to capture spatial and temporal relations for prediction [9, 10, 11]. However, these schemes are inherently uninterpretable

“black boxes” requiring large training data to tune millions of parameters. They are also fragile to *covariate shift* [12]: statistical mismatch between training and testing data.

*Graph attention networks* (GAT) [13] and *graph transformers* [14] are adaptations of the basic self-attention mechanism in transformers for graph-structured data (e.g., computing output embeddings using only input embeddings in local graph neighborhoods). However, they are still intrinsically uninterpretable and maintain large parameter sizes.

In contrast, *algorithm unrolling* [15] offers an alternative hybrid model-based / data-driven paradigm; by “unrolling” iterations of a model-based algorithm minimizing a well-defined optimization objective into neural layers stacked together to form a feed-forward network for data-driven parameter learning via back-propagation, the resulting network can be *both* mathematically interpretable *and* competitive in performance to state-of-the-art (SOTA) DL models. As examples, Yang et al. [16], Yu et al. [17] design optimization algorithms that unroll into transformer-like neural nets. Inspired by Yu et al. [17] and extending from Thuc et al. [18]<sup>1</sup>, we *unroll a dual-graph-based optimization algorithm into a lightweight interpretable transformer-like neural net for the traffic forecast problem*.

Specifically, we propose a novel *mixed-graph* approach and learn undirected graph  $\mathcal{G}^u$  and directed graph  $\mathcal{G}^d$  from data, to capture spatial correlations across geography and sequential relationships over time, respectively. We show that our graph learning modules are akin to the basic self-attention mechanism [19], and thus our unrolled graph-based neural nets are transformers. Given the two learned graphs, we define a prediction objective for future samples in signal  $\mathbf{x}$ , assuming  $\mathbf{x}$  is “smooth” with respect to (w.r.t.) both  $\mathcal{G}^u$  and  $\mathcal{G}^d$  in variational terms: *graph Laplacian regularizer* (GLR) [20] for undirected  $\mathcal{G}^u$ , and newly designed *directed graph Laplacian regularizer* (DGLR) and *directed graph total variation* (DGTV) for directed  $\mathcal{G}^d$ . We construct a corresponding iterative optimization algorithm based on *alternating direction method of multipliers* (ADMM) [21] that unrolls into neural layers for parameter learning. **For the first time, our proposed DGLR and DGTV variational terms quantify and promote signal smoothness on a directed graph, with intuitive low-pass filter interpretations.** Experiments show that our unrolled networks achieve competitive traffic forecast performance as SOTA prediction schemes, while employing drastically fewer parameters (**6.4% of transformer-based PDFormer** [22]).

## 2 Preliminaries

**Undirected Graph Definitions:** Denote by  $\mathcal{G}^u(\mathcal{V}, \mathcal{E}^u, \mathbf{W}^u)$  an *undirected* graph with node set  $\mathcal{V} = \{1, \dots, N\}$  and undirected edge set  $\mathcal{E}^u$ , where  $(i, j) \in \mathcal{E}^u$  implies that an undirected edge exists connecting nodes  $i$  and  $j$  with weight  $w_{i,j}^u = W_{i,j}^u$ , and  $(i, j) \notin \mathcal{E}^u$  implies  $W_{i,j}^u = 0$ .  $\mathbf{W}^u \in \mathbb{R}^{N \times N}$  is the symmetric *adjacency matrix* for  $\mathcal{G}^u$ . Denote by  $\mathbf{D}^u \in \mathbb{R}^{N \times N}$  a diagonal *degree matrix*, where  $D_{i,i}^u = \sum_j W_{j,i}^u$ . The symmetric *graph Laplacian matrix* is  $\mathbf{L}^u \triangleq \mathbf{D}^u - \mathbf{W}^u$  [3].  $\mathbf{L}^u$  is *positive semi-definite* (PSD) if all edge weights are non-negative  $w_{i,j}^u \geq 0, \forall i, j$  [4]. The symmetric *normalized graph Laplacian matrix* is  $\mathbf{L}_n^u \triangleq \mathbf{I} - (\mathbf{D}^u)^{-1/2} \mathbf{W}^u (\mathbf{D}^u)^{-1/2}$ , while the asymmetric *random-walk graph Laplacian matrix* is  $\mathbf{L}_r^u \triangleq \mathbf{I} - (\mathbf{D}^u)^{-1} \mathbf{W}^u$ .

One can define a *graph spectrum* by eigen-decomposing the real and symmetric graph Laplacian  $\mathbf{L}^u$  (or normalized graph Laplacian  $\mathbf{L}_n^u$ ), where the  $k$ -th eigen-pair  $(\lambda_k, \mathbf{v}_k)$  is interpreted as the  $k$ -th graph frequency and Fourier mode, respectively [3]. Given  $\{\mathbf{v}_k\}$  are orthonormal vectors, one can decompose a signal  $\mathbf{x}$  into its graph frequency components as  $\boldsymbol{\alpha} = \mathbf{V}^\top \mathbf{x}$ , where  $\mathbf{L}^u = \mathbf{V} \text{diag}(\{\lambda_k\}) \mathbf{V}^\top$ , and  $\mathbf{V}^\top$  is the *graph Fourier transform* (GFT).

The  $\ell_2$ -norm *graph Laplacian regularizer* (GLR) [20],  $\mathbf{x}^\top \mathbf{L}^u \mathbf{x} = \sum_{(i,j) \in \mathcal{E}^u} w_{i,j}^u (x_i - x_j)^2$ , is used to regularize an ill-posed signal restoration problem, like denoising, to bias low-frequency signal reconstruction (i.e., signals consistent with similarity graph  $\mathcal{G}^u$ ) given observation  $\mathbf{y}$ :

$$\begin{aligned} \mathbf{x}^* &= \arg \min_{\mathbf{x}} \|\mathbf{y} - \mathbf{x}\|_2^2 + \mu \mathbf{x}^\top \mathbf{L}^u \mathbf{x} \\ &= (\mathbf{I} + \mu \mathbf{L}^u)^{-1} \mathbf{y} = \mathbf{V} \text{diag} \left( \frac{1}{1 + \mu \lambda_1}, \dots, \frac{1}{1 + \mu \lambda_N} \right) \mathbf{V}^\top \mathbf{y}. \end{aligned} \quad (1)$$

<sup>1</sup>While Thuc et al. [18] focuses on unrolling of *undirected*-graph-based algorithms into transformer-like neural nets for image interpolation, we extend the study to *mixed* graphs with both undirected and directed edges to capture spatial and temporal pairwise relations, respectively, for traffic forecast.

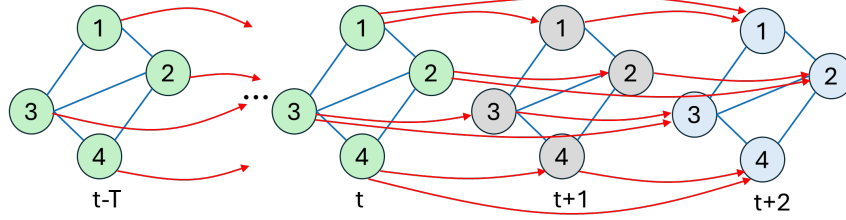


Figure 1: Example of a mixed graph with undirected edges (blue) connecting nodes of the same time instants, and directed edges (red) connecting nodes at  $t$  to nodes in window  $\{t+1, t+2\}$ .

$\mu$  is a bias-variance tradeoff parameter [23], and the low-pass filter response is  $f(\lambda) = (1 + \mu\lambda)^{-1}$ .

**Directed Graph Definitions:** We define analogous notations for a *directed* graph, denoted by  $\mathcal{G}^d(\mathcal{V}, \mathcal{E}^d, \mathbf{W}^d)$ .  $[i, j] \in \mathcal{E}^d$  implies a directed edge exists from node  $i$  to  $j$  with weight  $w_{j,i}^d = W_{j,i}^d$ .  $\mathbf{W}^d \in \mathbb{R}^{N \times N}$  is the asymmetric *adjacency matrix*. Denote by  $\mathbf{D}^d \in \mathbb{R}^{N \times N}$  a diagonal *in-degree matrix*, where  $D_{i,i}^d = \sum_j W_{i,j}^d$ . The *directed graph Laplacian* matrix is defined as  $\mathbf{L}^d \triangleq \mathbf{D}^d - \mathbf{W}^d$ . The *directed random-walk graph Laplacian* matrix is  $\mathbf{L}_r^d \triangleq \mathbf{I} - (\mathbf{D}^d)^{-1} \mathbf{W}^d$ .

Similar frequency notion cannot be simply defined for directed graphs via eigen-decomposition of directed graph Laplacian  $\mathbf{L}^d$ , because  $\mathbf{L}^d$  is asymmetric, and thus the Spectral Theorem [24] does not apply. We circumvent this problem by designing new variational terms in Section 3.2.

### 3 Optimization Formulation & Algorithm

#### 3.1 Mixed Graph for Spatial/Temporal Data

We describe the construction of a mixed graph for spatial/temporal data. A measurement station  $i$  observes samples  $x_i^{t-T}, \dots, x_i^t$  at past and present instants  $t-T, \dots, t$  and samples  $x_i^{t+1}, \dots, x_i^{t+S}$  at future instants  $t+1, \dots, t+S$ . Denote by  $\mathbf{x} = [\mathbf{x}^{t-T}; \dots; \mathbf{x}^{t+S}] \in \mathbb{R}^{N(T+S+1)}$  the target graph signal—a concatenation of samples from all  $N$  nodes across all  $T+S+1$  instants. A *product graph*  $\mathcal{G}$  of  $N \times (T+S+1)$  nodes represents samples at  $T+S+1$  instants.  $\mathcal{G}$  is a mixture of: i) undirected graph  $\mathcal{G}^u$  connecting spatially node pairs of the same instants, and ii) directed graph  $\mathcal{G}^d$  connecting temporally each node  $i$  at instant  $\tau$  to the same node at instants  $\tau+1, \dots, \tau+W$ , where  $W$  denotes the pre-defined *time window*. See Fig. 1 for an illustration of a mixed graph with undirected spatial edges (blue) and directed temporal edges (red) for  $W=2$ .

#### 3.2 Variational Terms for Directed Graphs

Our constructed  $\mathcal{G}^d$  is a *directed acyclic graph* (DAG); a directed edge always stems from a node at instant  $\tau$  to a node at a future instant  $\tau+s$ , and thus no cycles exist. We first define a symmetric variational term for  $\mathcal{G}^d$  called *directed graph Laplacian regularizer* (DGLR) to quantify variation of a signal  $\mathbf{x}$  on  $\mathcal{G}^d$ . Denote by  $\mathcal{S} \subset \mathcal{N}$  the set of *source nodes* with zero in-degrees, and  $\bar{\mathcal{S}} \triangleq \mathcal{N} \setminus \mathcal{S}$  its complement. First, we add a self-loop of weight 1 to each node in  $\bar{\mathcal{S}}$ ; this ensures that  $(\mathbf{D}^d)^{-1}$  is well-defined. Next, we define the row-stochastic *random-walk adjacency matrix*  $\mathbf{W}_r^d \triangleq (\mathbf{D}^d)^{-1} \mathbf{W}^d$ .

##### 3.2.1 $\ell_2$ -norm Variational Term

Interpreting  $\mathbf{W}_r^d$  as a *graph shift operator* (GSO) [25] on  $\mathcal{G}^d$ , we first define an  $\ell_2$ -norm variational term<sup>2</sup> for  $\mathcal{G}^d$  as the squared difference between  $\mathbf{x}$  and its graph-shifted version  $\mathbf{W}_r^d \mathbf{x}$ :

$$\|\mathbf{x} - \mathbf{W}_r^d \mathbf{x}\|_2^2 = \|(\mathbf{I} - \mathbf{W}_r^d) \mathbf{x}\|_2^2 = \mathbf{x}^\top \underbrace{(\mathbf{L}_r^d)^\top \mathbf{L}_r^d}_{\mathcal{L}_r^d} \mathbf{x} \quad (2)$$

<sup>2</sup>A similar directed graph variational term was defined in Li et al. [26] towards an objective for directed graph sampling. We focus instead on directed graph signal restoration.

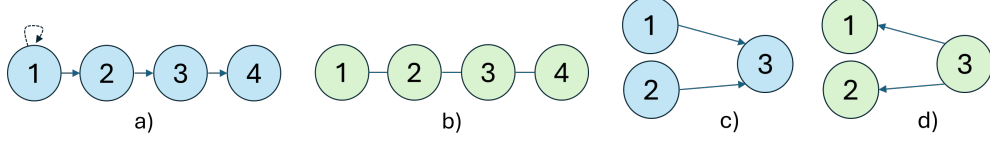


Figure 2: Example of a 4-node DAG  $\mathcal{G}^d$ , with an added self-loop at node 1, specified by  $\mathbf{L}_r^d$  (a), and corresponding undirected graph  $\mathcal{G}^u$ , specified by  $\mathcal{L}_r^d = (\mathbf{L}_r^d)^\top \mathbf{L}_r^d = \mathbf{L}^u$  (b). Example of a 3-node DAG (c), and a 3-node DAG with opposite directional edges (d).

where *symmetrized directed graph Laplacian* matrix  $\mathcal{L}_r^d \triangleq (\mathbf{L}_r^d)^\top \mathbf{L}_r^d$  is symmetric and PSD. We call  $\mathbf{x}^\top \mathcal{L}_r^d \mathbf{x}$  the DGLR, which computes the sum of squared differences between each child  $j \in \bar{\mathcal{S}}$  and its parents  $i$  for  $[i, j] \in \mathcal{E}^d$ . Note that DGLR computes to zero for the constant vector  $\mathbf{1}$ :

$$\mathbf{1}^\top \mathcal{L}_r^d \mathbf{1} = \mathbf{1}^\top (\mathbf{L}_r^d)^\top \mathbf{L}_r^d \mathbf{1} = \mathbf{1}^\top (\mathbf{L}_r^d)^\top (\mathbf{I} - \mathbf{W}_r^d) \mathbf{1} \stackrel{(a)}{=} \mathbf{0}$$

where (a) follows from  $\mathbf{W}_r^d$  being row-stochastic. This makes sense, as constant  $\mathbf{1}$  is the smoothest signal and has no variation across any graph kernels.

We interpret eigen-pairs  $\{(\xi_k, \mathbf{u}_k)\}$  of  $\mathcal{L}_r^d$  as graph frequencies and graph Fourier modes for directed graph  $\mathcal{G}^d$ , respectively, similar to eigen-pairs  $\{(\lambda_k, \mathbf{v}_k)\}$  of graph Laplacian  $\mathbf{L}^u$  for an undirected graph. Importantly, we prove that our frequency definition using DGLR defaults to pure sinusoids as frequencies in the unweighted directed line graph case. Thus, our algorithm minimizing DGLR includes TVSP schemes like Ramakrishna et al. [2] that analyze signals along the time dimension using classical Fourier filters as special cases.

**Theorem 3.1.** *Consider a directed line graph  $\mathcal{G}^d$  of  $N$  nodes with directed edge weights equal to 1, where the first (source) node is augmented with a self-loop of weight 1. The symmetrized directed graph Laplacian  $\mathcal{L}_r^d = (\mathbf{L}_r^d)^\top \mathbf{L}_r^d$ , where  $\mathbf{L}_r^d$  is the random-walk graph Laplacian for  $\mathcal{G}^d$ , is the same as graph Laplacian  $\mathbf{L}^u$  for an undirected line graph  $\mathcal{G}^u$  of  $N$  nodes with edge weights equal to 1.*

See Appendix A for a formal proof.

**Remark:** Using our symmetrized  $\mathcal{L}_r^d$  does not mean directionality has been lost. For the 3-node DAG in Fig. 2(c), the variational term is  $\|\mathbf{L}_r^d \mathbf{x}\|_2^2 = (x_3 - \frac{1}{2}(x_1 + x_2))^2$  and computes to 0 for  $\mathbf{x} = [2 \ 0 \ 1]^\top$ . On the other hand, for the DAG in Fig. 2(d) with opposite directions, the variational term is  $\|\mathbf{L}_r^d \mathbf{x}\|_2^2 = (x_1 - x_3)^2 + (x_2 - x_3)^2$  and computes to 0 only if  $\mathbf{x}$  is a constant vector.

### 3.2.2 $\ell_1$ -Norm Variational Term

Using  $\mathbf{W}_r^d$  again as a GSO, we define an  $\ell_1$ -norm variational term called *directed graph total variation* (DGTV) as

$$\|\mathbf{x} - \mathbf{W}_r^d \mathbf{x}\|_1 = \|\mathbf{L}_r^d \mathbf{x}\|_1 = \sum_{j \in \bar{\mathcal{S}}} |x_j - \sum_i w_{j,i} x_i|. \quad (3)$$

Unlike DGLR in (2), DGTV is not symmetric and has no obvious frequency interpretation. Nonetheless, we provide a *two-channel filterbank* interpretation in the sequel.

## 3.3 Optimization Formulation

Denote by  $\mathbf{y} \in \mathbb{R}^M$  the observation,  $\mathbf{x} \in \mathbb{R}^{N(T+S+1)}$  the target signal, and  $\mathbf{H} \in \{0, 1\}^{M \times N(T+S+1)}$  the sampling matrix that selects  $M$  observed samples from  $N(T+S+1)$  entries in  $\mathbf{x}$ . Given defined undirected and directed edges, we write an objective for  $\mathbf{x}$  containing a squared-error fidelity term and graph smoothness terms for the two graphs  $\mathcal{G}^u$  and  $\mathcal{G}^d$ —GLR, DGLR, and DGTV:

$$\min_{\mathbf{x}} \|\mathbf{y} - \mathbf{H} \mathbf{x}\|_2^2 + \mu_u \mathbf{x}^\top \mathbf{L}^u \mathbf{x} + \mu_{d,2} \mathbf{x}^\top \mathcal{L}_r^d \mathbf{x} + \mu_{d,1} \|\mathbf{L}_r^d \mathbf{x}\|_1 \quad (4)$$

where  $\mu_u, \mu_{d,2}, \mu_{d,1} \in \mathbb{R}_+$  are weight parameters for the three regularization terms. Combination of  $\ell_2$ - and  $\ell_1$ -norm penalties—DGLR and DGTV for directed graph  $\mathcal{G}^d$  in our case<sup>3</sup>—is called *elastic*

<sup>3</sup>We can employ both  $\ell_2$ - and  $\ell_1$ -norm regularization terms for the undirected graph  $\mathcal{G}^u$  as well. For simplicity, we focus on designing new regularization terms for directed graphs in this paper.

*net regularization* in statistics [27] with demonstrable improved robustness. Further, employing both regularization terms means that, after algorithm unrolling, we can adapt an appropriate mixture by learning weights  $\mu_{d,2}$  and  $\mu_{d,1}$  per neural layer.

(4) is a convex minimization problem composed of convex smooth  $\ell_2$ -norm terms and one convex non-smooth  $\ell_1$ -norm term. We pursue a divide-and-conquer approach and solve (4) via an ADMM framework [21] by minimizing  $\ell_2$ - and  $\ell_1$ -norm terms in (4) alternately.

### 3.4 ADMM Optimization Algorithm

We first introduce *auxiliary variable*  $\phi$  and rewrite the optimization in (4) as

$$\min_{\mathbf{x}, \phi} \|\mathbf{y} - \mathbf{H}\mathbf{x}\|_2^2 + \mu_u \mathbf{x}^\top \mathbf{L}^u \mathbf{x} + \mu_{d,2} \mathbf{x}^\top \mathcal{L}_r^d \mathbf{x} + \mu_{d,1} \|\phi\|_1, \quad \text{s.t. } \phi = \mathbf{L}_r^d \mathbf{x}. \quad (5)$$

Using the augmented Lagrangian method [28], we rewrite (5) in an unconstrained form:

$$\min_{\mathbf{x}, \phi} \|\mathbf{y} - \mathbf{H}\mathbf{x}\|_2^2 + \mu_u \mathbf{x}^\top \mathbf{L}^u \mathbf{x} + \mu_{d,2} \mathbf{x}^\top \mathcal{L}_r^d \mathbf{x} + \mu_{d,1} \|\phi\|_1 + \gamma^\top (\phi - \mathbf{L}_r^d \mathbf{x}) + \frac{\rho}{2} \|\phi - \mathbf{L}_r^d \mathbf{x}\|_2^2 \quad (6)$$

where  $\gamma \in \mathbb{R}^{N(T+S+1)}$  is a Lagrange multiplier vector, and  $\rho \in \mathbb{R}_+$  is a non-negative ADMM parameter. We solve (6) iteratively by minimizing variables  $\mathbf{x}$  and  $\phi$  in alternating steps till convergence.

#### 3.4.1 Minimizing $\mathbf{x}^{\tau+1}$

Fixing  $\phi^\tau$  and  $\gamma^\tau$  at iteration  $\tau$ , optimization in (6) for  $\mathbf{x}^{\tau+1}$  becomes an unconstrained convex quadratic objective. The solution is a system of linear equations:

$$\left( \mathbf{H}^\top \mathbf{H} + \mu_u \mathbf{L}^u + (\mu_{d,2} + \frac{\rho}{2}) \mathcal{L}_r^d \right) \mathbf{x}^{\tau+1} = (\mathbf{L}_r^d)^\top \left( \frac{\rho}{2} \phi^\tau + \frac{\gamma^\tau}{2} \right) + \mathbf{H}^\top \mathbf{y}. \quad (7)$$

Because coefficient matrix  $\mathbf{H}^\top \mathbf{H} + \mu_u \mathbf{L}^u + (\mu_{d,2} + \frac{\rho}{2}) \mathcal{L}_r^d$  is sparse, symmetric and PD, (7) can be solved in linear time via *conjugate gradient* (CG) [29] without matrix inversion.

**Splitting  $\ell_2$ -norm Terms:** Instead of solving (7) directly for  $\mathbf{x}^{\tau+1}$  at iteration  $\tau$ , we introduce again auxiliary variables  $\mathbf{z}_u$  and  $\mathbf{z}_d$  in (5) for the  $\ell_2$ -norm GLR and DGLR terms respectively, and rewrite the optimization as

$$\min_{\mathbf{x}, \mathbf{z}_u, \mathbf{z}_d} \|\mathbf{y} - \mathbf{H}\mathbf{x}\|_2^2 + \mu_u \mathbf{z}_u^\top \mathbf{L}^u \mathbf{z}_u + \mu_{d,2} \mathbf{z}_d^\top \mathcal{L}_r^d \mathbf{z}_d + (\gamma^\tau)^\top (\phi^\tau - \mathbf{L}_r^d \mathbf{x}) + \frac{\rho}{2} \|\phi^\tau - \mathbf{L}_r^d \mathbf{x}\|_2^2 \quad (8)$$

s.t.  $\mathbf{x} = \mathbf{z}_u = \mathbf{z}_d$ .

Using again the augmented Lagrangian method, we rewrite the unconstrained version as

$$\min_{\mathbf{x}, \mathbf{z}_u, \mathbf{z}_d} \|\mathbf{y} - \mathbf{H}\mathbf{x}\|_2^2 + \mu_u \mathbf{z}_u^\top \mathbf{L}^u \mathbf{z}_u + \mu_{d,2} \mathbf{z}_d^\top \mathcal{L}_r^d \mathbf{z}_d + (\gamma^\tau)^\top (\phi^\tau - \mathbf{L}_r^d \mathbf{x}) + \frac{\rho}{2} \|\phi^\tau - \mathbf{L}_r^d \mathbf{x}\|_2^2 \quad (9)$$

+  $(\gamma_u^\tau)^\top (\mathbf{x} - \mathbf{z}_u) + \frac{\rho_u}{2} \|\mathbf{x} - \mathbf{z}_u\|_2^2 + (\gamma_d^\tau)^\top (\mathbf{x} - \mathbf{z}_d) + \frac{\rho_d}{2} \|\mathbf{x} - \mathbf{z}_d\|_2^2$

where  $\gamma_u, \gamma_d \in \mathbb{R}^{N(T+S+1)}$  are multipliers, and  $\rho_u, \rho_d \in \mathbb{R}_+$  are ADMM parameters. Optimizing  $\mathbf{x}, \mathbf{z}_u$  and  $\mathbf{z}_d$  in (9) in turn at iteration  $\tau$  lead to three linear systems:

$$\left( \mathbf{H}^\top \mathbf{H} + \frac{\rho}{2} \mathcal{L}_r^d + \frac{\rho_u + \rho_d}{2} \mathbf{I} \right) \mathbf{x}^{\tau+1} = (\mathbf{L}_r^d)^\top \left( \frac{\gamma^\tau}{2} + \frac{\rho}{2} \phi^\tau \right) - \frac{\gamma_u^\tau}{2} + \frac{\rho_u}{2} \mathbf{z}_u^\tau - \frac{\gamma_d^\tau}{2} + \frac{\rho_d}{2} \mathbf{z}_d^\tau + \mathbf{H}^\top \mathbf{y} \quad (10)$$

$$\left( \mu_u \mathbf{L}^u + \frac{\rho_u}{2} \mathbf{I} \right) \mathbf{z}_u^{\tau+1} = \frac{\gamma_u^\tau}{2} + \frac{\rho_u}{2} \mathbf{x}^{\tau+1} \quad (11)$$

$$\left( \mu_{d,2} \mathcal{L}_r^d + \frac{\rho_d}{2} \mathbf{I} \right) \mathbf{z}_d^{\tau+1} = \frac{\gamma_d^\tau}{2} + \frac{\rho_d}{2} \mathbf{x}^{\tau+1}. \quad (12)$$

Thus, instead of solving (7) for  $\mathbf{x}^{\tau+1}$  directly at iteration  $\tau$ ,  $\mathbf{x}^{\tau+1}$ ,  $\mathbf{z}_u^{\tau+1}$  and  $\mathbf{z}_d^{\tau+1}$  are optimized in turn via (10) through (12) using CG. This splitting induces more network parameters for data-driven learning after algorithm unrolling (see Section 4.1) towards better performance, and affords us spectral filter interpretations of the derived linear systems.

**Interpretation:** To interpret solution  $\mathbf{z}_u^{\tau+1}$  spectrally, we rewrite (11) as

$$\mathbf{z}_u^{\tau+1} = \left( \frac{2\mu_u}{\rho_u} \mathbf{L}^u + \mathbf{I} \right)^{-1} \left( \frac{\gamma_u}{\rho_u} + \mathbf{x}^{\tau+1} \right) = \mathbf{V} \text{diag} \left( \left\{ \frac{1}{1 + \frac{2\mu_u}{\rho_u} \lambda_k} \right\} \right) \mathbf{V}^\top \left( \frac{\gamma_u}{\rho_u} + \mathbf{x}^{\tau+1} \right) \quad (13)$$

where  $\mathbf{L}^u = \mathbf{V} \text{diag}(\{\lambda_k\}) \mathbf{V}^\top$  is the eigen-decomposition. Thus, using frequencies defined by eigen-pairs  $\{(\lambda_k, \mathbf{v}_k)\}$  of  $\mathbf{L}^u$ ,  $\mathbf{z}_u^{\tau+1}$  is the *low-pass* filter output of  $\mathbf{x}^{\tau+1}$  offset by  $\frac{\gamma_u}{\rho_u}$ , with frequency response  $f(\lambda) = (1 + \frac{2\mu_u}{\rho_u} \lambda)^{-1}$ .

As done for  $\mathbf{z}_u^{\tau+1}$ , we can rewrite  $\mathbf{z}_d^{\tau+1}$  in (12) as

$$\mathbf{z}_d^{\tau+1} = \mathbf{U} \text{diag} \left( \left\{ \frac{1}{1 + \frac{2\mu_{d,2}}{\rho_d} \xi_k} \right\} \right) \mathbf{U}^\top \left( \frac{\gamma_d}{\rho_d} + \mathbf{x}^{\tau+1} \right) \quad (14)$$

where  $\mathcal{L}_r^d = \mathbf{U} \text{diag}(\{\xi_k\}) \mathbf{U}^\top$  is the eigen-decomposition. Analogously,  $\mathbf{z}_d^{\tau+1}$  is the *low-pass* filter output of  $\mathbf{x}^{\tau+1}$  offset by  $\frac{\gamma_d}{\rho_d}$ , with frequency response  $f(\xi) = (1 + \frac{2\mu_{d,2}}{\rho_d} \xi)^{-1}$ .

To interpret solution  $\mathbf{x}^{\tau+1}$  in (10) as a low-pass filter output, see Appendix B.

### 3.4.2 Minimizing $\phi^{\tau+1}$

Fixing  $\mathbf{x}^{\tau+1}$  at iteration  $\tau$ , optimizing  $\phi^{\tau+1}$  in (6) means

$$\phi^{\tau+1} = \arg \min_{\phi} g(\phi) = \mu_{d,1} \|\phi\|_1 + (\gamma^\tau)^\top (\phi - \mathbf{L}_r^d \mathbf{x}^{\tau+1}) + \frac{\rho}{2} \|\phi - \mathbf{L}_r^d \mathbf{x}^{\tau+1}\|_2^2. \quad (15)$$

(15) can be computed element-wise as follows (see Appendix C for a derivation):

$$\begin{aligned} \delta &= (\mathbf{L}_r^d)_i \mathbf{x}^{\tau+1} - \rho^{-1} \gamma_i^\tau \\ \phi_i^{\tau+1} &= \text{sign}(\delta) \cdot \max(|\delta| - \rho^{-1} \mu_{d,1}, 0). \end{aligned} \quad (16)$$

**Interpretation:** Soft-thresholding in (16) to compute  $\phi_i^{\tau+1}$  *attenuates* the  $i$ -th entry of  $\mathbf{L}_r^d \mathbf{x}^{\tau+1}$ . Given that graph Laplacians—second difference matrices on graphs—are high-pass filters [3], we interpret  $\mathbf{L}_r^d$  as the *high-pass channel* of a two-channel filterbank [30], where the corresponding *low-pass channel* is  $\mathbf{I} - \mathbf{L}_r^d = \mathbf{W}_r^d$ . Using (16) for processing means that the low-pass channel  $\mathbf{W}_r^d$  is unused and thus preserved. For example, the constant (low-frequency) signal  $\mathbf{1}$  passes through the low-pass channel undisturbed, *i.e.*,  $\mathbf{1} = \mathbf{W}_r^d \mathbf{1}$ , while it is filtered out completely by the high-pass channel, *i.e.*,  $\mathbf{0} = \mathbf{L}_r^d \mathbf{1}$ . Thus, attenuation of the high-pass channel means (16) is a low-pass filter.

### 3.4.3 Updating Lagrange Multipliers

For objective (6), we follow standard ADMM procedure to update Lagrange multiplier  $\gamma^{\tau+1}$  after each computation of  $\mathbf{x}^{\tau+1}$  and  $\phi^{\tau+1}$ :

$$\gamma^{\tau+1} = \gamma^\tau + \rho(\phi^{\tau+1} - \mathbf{L}_r^d \mathbf{x}^{\tau+1}). \quad (17)$$

Splitting the  $\ell_2$ -norm terms means that additional multipliers  $\gamma_u^{\tau+1}$  and  $\gamma_d^{\tau+1}$  in objective (9) must also be updated after each computation of  $\mathbf{x}^{\tau+1}$ ,  $\mathbf{z}_u^{\tau+1}$ ,  $\mathbf{z}_d^{\tau+1}$ , and  $\phi^{\tau+1}$ :

$$\gamma_u^{\tau+1} = \gamma_u^\tau + \rho_u(\mathbf{x}^{\tau+1} - \mathbf{z}_u^{\tau+1}), \quad \gamma_d^{\tau+1} = \gamma_d^\tau + \rho_d(\mathbf{x}^{\tau+1} - \mathbf{z}_d^{\tau+1}). \quad (18)$$

The ADMM loop is repeated till  $\mathbf{x}^{\tau+1}$  and  $\phi^{\tau+1}$  converge.

## 4 Unrolled Neural Network

We unroll our iterative ADMM algorithm to an interpretable neural net. The crux to our unrolled neural net is two periodically inserted graph learning modules for undirected and directed edge weight computation that are akin to the self-attention mechanism in classical transformers [19].

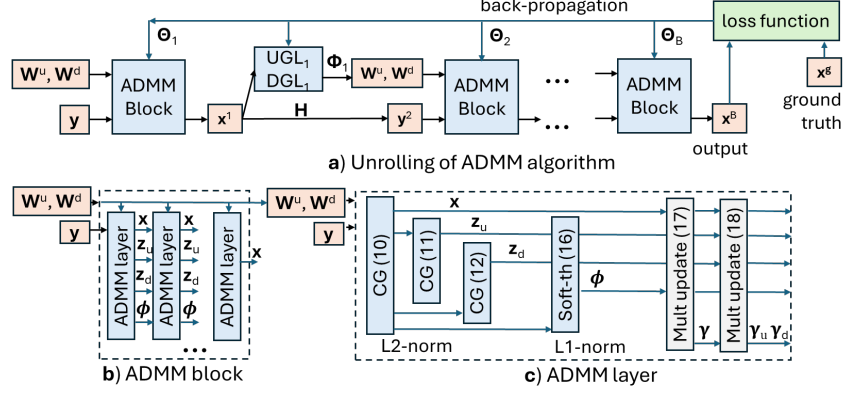


Figure 3: Unrolling of proposed iterative ADMM algorithm into blocks and neural layers.

#### 4.1 ADMM Algorithm Unrolling

We implement each iteration of our algorithm in Section 3.4 as a neural layer. Specifically, each ADMM iteration is implemented as four sub-layers in sequence: solving linear systems (10) for  $\mathbf{x}^{\tau+1}$ , (11) for  $\mathbf{z}_u^{\tau+1}$ , and (12) for  $\mathbf{z}_d^{\tau+1}$  via CG, and computing  $\phi^{\tau+1}$  via (16). CG is itself an iterative descent algorithm, where parameters  $\alpha$  and  $\beta$  corresponding to step size and momentum can be tuned end-to-end (see Appendix D for detailed implementation). Weight parameters  $\mu_u, \mu_{d,2}, \mu_{d,1}$  for prior terms and ADMM parameters  $\rho, \rho_u, \rho_d$  are also tuned per layer. Multipliers  $\gamma^{\tau+1}, \gamma_u^{\tau+1}, \gamma_d^{\tau+1}$  are then updated via (17) and (18) to complete one layer. Parameters learned during back-propagation for each ADMM block  $b$  are denoted by  $\Theta_b$ . See Fig. 3 for an illustration.

#### 4.2 Self-Attention Operator in Transformer

We first review the basic self-attention mechanism: a scaled dot product following by a softmax operation [19]. Denote by  $\mathbf{x}_i \in \mathbb{R}^E$  an *embedding* for token  $i$ . The *affinity* between tokens  $i$  and  $j$ ,  $e(i, j)$ , is the dot product of linear-transformed  $\mathbf{K}\mathbf{x}_i$  and  $\mathbf{Q}\mathbf{x}_j$ , where  $\mathbf{Q}, \mathbf{K} \in \mathbb{R}^{E \times E}$  are the *query* and *key* matrices, respectively. Using softmax, non-negative *attention weight*  $a_{i,j}$  is computed from  $e(i, j)$ 's as

$$a_{i,j} = \frac{\exp(e(i, j))}{\sum_{l=1}^N \exp(e(i, l))}, \quad e(i, j) = (\mathbf{Q}\mathbf{x}_j)^\top (\mathbf{K}\mathbf{x}_i). \quad (19)$$

Given attention weights  $a_{i,j}$ , output embedding  $\mathbf{y}_i$  for token  $i$  is computed as

$$\mathbf{y}_i = \sum_{l=1}^N a_{i,l} \mathbf{x}_l \mathbf{V} \quad (20)$$

where  $\mathbf{V} \in \mathbb{R}^{E \times E}$  is a *value* matrix. By “self-attention”, we mean that output embeddings are computed from weighted input embeddings. A transformer is thus a sequence of embedding-to-embedding mappings via self-attention operations defined by learned  $\mathbf{Q}, \mathbf{K}$  and  $\mathbf{V}$  matrices.

#### 4.3 Graph Learning Modules

**Undirected Graph Learning:** We learn an undirected graph  $\mathcal{G}^u$  in a module  $\text{UGL}_b$  at block  $b$ . For each node  $i$ , we compute a low-dimensional feature vector  $\mathbf{f}_i^u = F^u(\mathbf{e}_i) \in \mathbb{R}^K$ , where  $\mathbf{e}_i \in \mathbb{R}^E$  is a vector of signal values, position embeddings in time and Laplacian embeddings of the physical graph as done in Feng and Tassiulas [9], and  $F^u(\cdot)$  is a chosen learned nonlinear *feature function*  $F^u : \mathbb{R}^E \mapsto \mathbb{R}^K$ , e.g., a shallow GNN (see Appendix E.3 for details). As done in Thuc et al. [18], the feature distance between nodes  $i$  and  $j$  is computed as the *Mahalanobis distance*  $d^u(i, j)$ :

$$d^u(i, j) = (\mathbf{f}_i^u - \mathbf{f}_j^u)^\top \mathbf{M} (\mathbf{f}_i^u - \mathbf{f}_j^u) \quad (21)$$

where  $\mathbf{M} \succeq 0$  is a symmetric PSD *metric matrix* of dimension  $\mathbb{R}^{K \times K}$ . Distance in (21) is non-negative and *symmetric*, i.e.,  $d^u(i, j) = d^u(j, i)$ . Weight  $w_{i,j}^u$  of undirected edge  $(i, j) \in \mathcal{E}^u$  is computed as

$$w_{i,j}^u = \frac{\exp(-d^u(i, j))}{\sqrt{\sum_{l \in \mathcal{N}_i} \exp(-d^u(i, l))} \sqrt{\sum_{k \in \mathcal{N}_j} \exp(-d^u(k, j))}} \quad (22)$$

where the denominator summing over 1-hop neighborhood  $\mathcal{N}_i$  is inserted for normalization.

**Remark:** Interpreting distance  $d^u(i, j)$  as  $-e(i, j)$ , edge weights  $w_{i,j}^u$ 's in (22) are essentially attention weights  $a_{i,j}$ 's in (19), and thus the undirected graph learning module constitutes a self-attention mechanism, albeit requiring fewer parameters, since parameters for function  $F^u(\cdot)$  and metric matrix  $\mathbf{M}$  can be much smaller than large and dense query and key matrices,  $\mathbf{Q}$  and  $\mathbf{K}$ . Further, there is no value matrix  $\mathbf{V}$  required, since the output signal  $\mathbf{x}^{\tau+1}$  is computed through a set of low-pass filters—(10), (11), (12) and (16)—derived from our optimization of objective (4).

**Directed Graph Learning:** Similarly, we learn a directed graph  $\mathcal{G}^d$  in a module  $\text{DGL}_b$  at block  $b$ . For each node  $i$ , we compute a feature vector  $\mathbf{f}_i^d = F^d(\mathbf{e}_i) \in \mathbb{R}^K$  using feature function  $F^d(\cdot)$ . Like (21), we compute Mahalanobis distance  $d^d(i, j)$  between nodes  $i$  and  $j$ , given feature vectors  $\mathbf{f}_i^d$  and  $\mathbf{f}_j^d$ , using a learned PSD metric matrix  $\mathbf{P}$ . Weight  $w_{j,i}^d$  of directed edge  $[i, j] \in \mathcal{E}^d$  is then computed using exponential functions and normalization, as done in (22) for an undirected edge.

Parameters learned via back-propagation by the two graph learning modules at block  $b$ —parameters of  $F^u(\cdot)$ ,  $F^d(\cdot)$ ,  $\mathbf{M}$  and  $\mathbf{P}$ —are denoted by  $\Phi_b$ .

## 5 Experiments

### 5.1 Experimental Setup

We evaluate our model's performance on traffic speed datasets METR-LA, PEMS-BAY [31], and traffic flow dataset PEMS03 [32], each of which contains traffic data with a sampling interval of 5 minutes in a local region, together with the real connections and distances (or travel cost) between sensors. We reduce the size of the original dataset by sub-sampling 1/3 of all data uniformly, and split it into training, validation, and test sets by 6:2:2. We predict the traffic speed/flow in the following 30/60 minutes (6/12 steps) from the previously observed 60 minutes (12 steps) for all datasets.

We restrict our model to learn a *sparse* graph based on the real road connections and a limited time window to model only the *local* spatial/temporal influence. For undirected graphs  $\mathcal{G}^u$ , we connect each node with its  $k$  nearest neighbors (NNs). We construct 5 ADMM blocks, each contains 25 ADMM layers, and insert a graph learning module before each ADMM block. We set feature dimensions  $K = 6$ , and stack vertically 4 graph learning modules to learn in parallel as an implementation of the *multi-head* attention mechanism. We minimize the Huber loss with  $\delta = 1$  for the *entire* reconstructed sequence and the groundtruths. See Appendix E for more details.

### 5.2 Experimental Results

Table 1: Comparison of RMSE/MAE/MAPE(%) metrics of our lightweight transformer to baseline models on 30/60-minute forecasting in PeMS03, METR-LA and PEMS-BAY datasets. We use **boldface** for the smallest error and underline the next 3 smallest errors.

Dataset & Horizon	PEMS03 (358 nodes, 547 edges)		METR-LA (207 nodes, 1315 edges)		PEMS-BAY (325 nodes, 2090 edges)	
	30 minutes	60 minutes	30 minutes	60 minutes	30 minutes	60 minutes
VAR [33]	28.07 / <u>16.53</u> / 17.49	30.54 / 18.31 / 19.61	10.72 / 5.55 / 11.29	12.59 / 6.99 / 13.46	3.81 / 2.08 / 4.46	<b>3.98</b> / 2.56 / 5.52
STGCN [34]	28.06 / 18.24 / 17.76	37.31 / 24.29 / 23.00	11.97 / 5.43 / 13.45	14.77 / 6.86 / 17.51	4.32 / 2.65 / 5.21	7.39 / 4.26 / 8.25
STSGCN [35]	<u>26.41</u> / <u>16.75</u> / <b>16.86</b>	30.62 / 19.35 / <u>19.15</u>	<u>10.25</u> / 4.05 / 9.18	12.65 / <u>5.18</u> / 11.48	<u>3.43</u> / <u>1.54</u> / <u>3.28</u>	<u>4.50</u> / <u>1.93</u> / <u>4.42</u>
ST-Wave [36]	<u>25.57</u> / 15.11 / <b>15.04</b>	28.65 / 16.81 / 19.24	10.81 / 4.11 / 9.16	13.24 / 5.33 / 11.32	<u>3.53</u> / <u>1.49</u> / 3.18	4.30 / <b>1.82</b> / <b>4.33</b>
ASTTN [9]	26.84 / 17.04 / 21.46	<u>27.24</u> / <b>16.43</b> / <b>15.63</b>	11.49 / 4.80 / 10.97	<b>11.10</b> / <u>5.08</u> / 12.51	5.07 / 2.23 / 4.65	4.82 / 2.13 / <u>4.40</u>
PDFormer [22]	<b>23.71</b> / <b>15.05</b> / 18.16	<b>27.16</b> / <u>17.26</u> / 21.21	<u>10.21</u> / <u>3.89</u> / <u>8.50</u>	<u>12.17</u> / <u>4.81</u> / <u>10.92</u>	<b>3.18</b> / <b>1.41</b> / <b>2.99</b>	<u>4.55</u> / <u>2.00</u> / 4.88
STAEformer [37]	30.22 / 18.85 / 26.62	38.36 / 23.68 / 29.21	<b>10.16</b> / <b>3.73</b> / <b>8.25</b>	<u>12.58</u> / <b>4.79</b> / <b>10.08</b>	4.07 / 1.75 / <u>3.95</u>	5.28 / 2.28 / 5.59
<b>Ours</b>	<u>26.10</u> / 17.03 / 18.85	<u>27.67</u> / <u>17.46</u> / <u>17.72</u>	<u>10.35</u> / 4.22 / 9.70	<u>12.37</u> / 5.27 / 11.91	<u>3.78</u> / <u>1.70</u> / 4.08	4.60 / <u>2.03</u> / <u>4.79</u>



Table 2: Comparison of the number of parameters between our model and baseline deep learning models for 60-minute forecasting in PEMS03 dataset.

Model	<b>Ours</b>	STGCN	STSGCN	ST-Wave	ASTTN	PDFormer	STAEformer
Params #	<b>34,096</b>	321,941	3,496,212	882,558	161,635	531,165	1,403,940

We train each run of our model on NVIDIA GeForce RTX 3090. We evaluate our unrolling model against model-based method VAR [33], GNN-based models STGCN<sup>4</sup> [34] and STSGCN [35], GAT-based models ST-Wave [36] and ASTTN [9], and transformer-based models PDFormer [22] and STAEformer [37] with 70 epochs of training on the reduced dataset with the Root Mean Squared Error (RMSE), Mean Absolute Error (MAE), and Mean Absolute Percentage Error (MAPE) in the predicted 6/12 steps.

Table 1 shows the performance of our models and baselines in traffic forecasting, and Table 2 compares the number of parameters. We observe that our models reach comparable performance to most baseline models, while employ drastically fewer parameters (**6.4% of transformer-based PDFormer**). Among all the models, ST-Wave generally achieves the best performance, which is attributed to an application-specific usage of wavelet transforms, but requires even more parameters than transformers. The largest model STSGCN fails to achieve satisfying performance for PEMS03, where the real connections are highly sparse. STAEformer, the largest transformer, also overfits heavily in the reduced PEMS03 and PEMS-BAY datasets. We also observe significant oscillations in validation loss during training in ASTTN due to the adaptive attention maps. *In summary, none of the DL-based baseline schemes unambiguously achieves the best performance across the three datasets, while all require significantly more parameters than our models.*

### 5.3 Ablation Study

Next, we discuss the effectiveness of the new directed graph priors, DGLR and DGTv, as well as the benefit of directed-graph modeling of temporal relations. First, we separately test the effects of DGLR and DGTv by removing the prior and unrolling the ADMM algorithm. We denote these models as “w/o DGTv” and “w/o DGLR”. To test the benefit of the directed-graph modeling, we change the temporal graph  $\mathcal{G}^d$  into a fully undirected graph  $\mathcal{G}^u$  while maintaining the connections, and replace the directed graph priors with a GLR prior  $\mathbf{x}^\top \mathbf{L}^n \mathbf{x}$  with the same coefficient  $\mu_n = \mu_{d,2}$ . We denote the undirected-time unrolling model as “UT”. Detailed derivations of the ADMM algorithm for all the above ablation studies are in Appendix F.

Table 3: Performance comparison in RMSE / MAE / MAPE(%) of the ablation studies of directed-graph modeling and directed graph priors in 60-minute forecasting with PEMS03 and METR-LA.

Dataset	Mixed-Graph	UT	w/o DGTv	w/o DGLR
PEMS03	27.67 / <b>17.46</b> / <b>17.72</b>	<b>27.52</b> / 17.87 / 18.82	27.78 / 17.85 / 17.90	30.89 / 20.02 / 21.10
METR-LA	12.37 / <b>5.27</b> / <b>11.91</b>	12.51 / 5.42 / 12.11	<b>12.36</b> / 5.40 / 12.31	12.41 / 5.35 / 12.20

As is summarized in Table 3, removing the DGLR or DGTv term leads to noticeable drops in performance, which underscores their importance as directed graph priors. Moreover, our model outperforms the fully-undirected-graph-based model, demonstrating that sequential relationships—such as time—are better modeled as directed graphs.

For further ablation studies in the number of nearest neighbors  $k$ , size of time window  $W$ , number of ADMM blocks and layers, and the splitting-term strategy in (8), see Appendix G.

## 6 Conclusion

To forecast city traffic, we unroll a mixed-graph optimization algorithm into a lightweight transformer-like neural net, where an undirected graph models spatial correlations and a directed graph models

<sup>4</sup>STGCN predicts only one time step at a time. We train the model to predict only the next step, and predict the entire sequence recursively.

temporal relationships. We show that the two graph learning modules are akin to the classical self-attention mechanism. We design new  $\ell_2$  and  $\ell_1$ -norm regularizers to quantify and promote signal smoothness on directed graphs. We interpret the derived processing operations from a constructed ADMM algorithm as low-pass filters. Experiments demonstrate competitive prediction performance at drastically reduced parameter counts. One limitation of our approach is that our computed Mahalanobis distances  $d^u(i, j)$  and  $d^d(i, j)$  for respective undirected and directed graphs are non-negative (due to learned PSD metric matrices  $\mathbf{M}$  and  $\mathbf{P}$ ), whereas affinity  $e(i, j)$  in traditional self-attention can be negative. We will study extensions to signed distances as future work.

## References

- [1] F. Grassi, A. Loukas, N. Perraudin, and B. Ricaud, “A time-vertex signal processing framework: Scalable processing and meaningful representations for time-series on graphs,” *IEEE Transactions on Signal Processing*, vol. 66, no. 3, pp. 817–829, 2018.
- [2] R. Ramakrishna, H.-T. Wai, and A. Scaglione, “A user guide to low-pass graph signal processing and its applications: Tools and applications,” *IEEE Signal Processing Magazine*, vol. 37, no. 6, pp. 74–85, 2020.
- [3] A. Ortega, P. Frossard, J. Kovacevic, J. M. F. Moura, and P. Vandergheynst, “Graph signal processing: Overview, challenges, and applications,” in *Proceedings of the IEEE*, vol. 106, no.5, May 2018, pp. 808–828.
- [4] G. Cheung, E. Magli, Y. Tanaka, and M. Ng, “Graph spectral image processing,” in *Proceedings of the IEEE*, vol. 106, no.5, May 2018, pp. 907–930.
- [5] V. Kalofolias, A. Loukas, D. Thanou, and P. Frossard, “Learning time varying graphs,” in *2017 IEEE International Conference on Acoustics, Speech and Signal Processing (ICASSP)*, 2017, pp. 2826–2830.
- [6] K. Yamada, Y. Tanaka, and A. Ortega, “Time-varying graph learning based on sparseness of temporal variation,” in *ICASSP 2019 - 2019 IEEE International Conference on Acoustics, Speech and Signal Processing (ICASSP)*, 2019, pp. 5411–5415.
- [7] S. Bagheri, G. Cheung, T. Eadie, and A. Ortega, “Joint signal interpolation / time-varying graph estimation via smoothness and low-rank priors,” in *ICASSP 2024 - 2024 IEEE International Conference on Acoustics, Speech and Signal Processing (ICASSP)*, 2024, pp. 9646–9650.
- [8] A. Vaswani, N. Shazeer, N. Parmar, J. Uszkoreit, L. Jones, A. N. Gomez, L. Kaiser, and I. Polosukhin, “Attention is all you need,” *Advances in neural information processing systems*, vol. 30, 2017.
- [9] A. Feng and L. Tassiulas, “Adaptive graph spatial-temporal transformer network for traffic forecasting,” in *Proceedings of the 31st ACM International Conference on Information & Knowledge Management*, ser. CIKM ’22. New York, NY, USA: Association for Computing Machinery, 2022, p. 3933–3937. [Online]. Available: <https://doi.org/10.1145/3511808.3557540>
- [10] Z. Gao, X. Shi, H. Wang, Y. Zhu, Y. B. Wang, M. Li, and D.-Y. Yeung, “Earthformer: Exploring space-time transformers for earth system forecasting,” in *Advances in Neural Information Processing Systems*, S. Koyejo, S. Mohamed, A. Agarwal, D. Belgrave, K. Cho, and A. Oh, Eds., vol. 35. Curran Associates, Inc., 2022, pp. 25 390–25 403. [Online]. Available: [https://proceedings.neurips.cc/paper\\_files/paper/2022/file/a2affd71d15e8fedffe18d0219f4837a-Paper-Conference.pdf](https://proceedings.neurips.cc/paper_files/paper/2022/file/a2affd71d15e8fedffe18d0219f4837a-Paper-Conference.pdf)
- [11] Q. Jin, X. Zhang, X. Xiao, Y. Wang, S. Xiang, and C. Pan, “Preformer: Simple and efficient design for precipitation nowcasting with transformers,” *IEEE Geoscience and Remote Sensing Letters*, vol. 21, pp. 1–5, 2024.
- [12] R. Zhang, S. Frei, and P. L. Bartlett, “Trained transformers learn linear models in-context,” *Journal of Machine Learning Research*, vol. 25, no. 49, pp. 1–55, 2024. [Online]. Available: <http://jmlr.org/papers/v25/23-1042.html>
- [13] P. Velickovic, G. Cucurull, A. Casanova, A. Romero, P. Lio, and Y. Bengio, “Graph attention networks,” 2018. [Online]. Available: <https://arxiv.org/abs/1710.10903>
- [14] V. P. Dwivedi and X. Bresson, “A generalization of transformer networks to graphs,” 2021. [Online]. Available: <https://arxiv.org/abs/2012.09699>
- [15] V. Monga, Y. Li, and Y. C. Eldar, “Algorithm unrolling: Interpretable, efficient deep learning for signal and image processing,” *IEEE Signal Processing Magazine*, vol. 38, no. 2, pp. 18–44, 2021.

- [16] Y. Yang, Z. Huang, and D. Wipf, “Transformers from an optimization perspective,” in *Proceedings of the 36th International Conference on Neural Information Processing Systems*, ser. NIPS ’22. Red Hook, NY, USA: Curran Associates Inc., 2024.
- [17] Y. Yu, S. Buchanan, D. Pai, T. Chu, Z. Wu, S. Tong, B. Haeffele, and Y. Ma, “White-box transformers via sparse rate reduction,” in *Advances in Neural Information Processing Systems*, A. Oh, T. Neumann, A. Globerson, K. Saenko, M. Hardt, and S. Levine, Eds., vol. 36. Curran Associates, Inc., 2023, pp. 9422–9457. [Online]. Available: [https://proceedings.neurips.cc/paper\\_files/paper/2023/file/1e118ba9ee76c20df728b42a35fb4704-Paper-Conference.pdf](https://proceedings.neurips.cc/paper_files/paper/2023/file/1e118ba9ee76c20df728b42a35fb4704-Paper-Conference.pdf)
- [18] T. Thuc, P. Eftekhari, S. A. Hosseini, G. Cheung, and P. A. Chou, “Interpretable lightweight transformer via unrolling of learned graph smoothness priors,” in *Advances in Neural Information Processing Systems*, A. Globerson, L. Mackey, D. Belgrave, A. Fan, U. Paquet, J. Tomczak, and C. Zhang, Eds., vol. 37. Curran Associates, Inc., 2024, pp. 6393–6416.
- [19] D. Bahdanau, K. Cho, and Y. Bengio, “Neural machine translation by jointly learning to align and translate,” *CoRR*, vol. abs/1409.0473, 2014. [Online]. Available: <https://api.semanticscholar.org/CorpusID:11212020>
- [20] J. Pang and G. Cheung, “Graph Laplacian regularization for inverse imaging: Analysis in the continuous domain,” in *IEEE Transactions on Image Processing*, vol. 26, no. 4, April 2017, pp. 1770–1785.
- [21] S. Boyd, N. Parikh, E. Chu, B. Peleato, and J. Eckstein, “Distributed optimization and statistical learning via the alternating direction method of multipliers,” in *Foundations and Trends in Optimization*, vol. 3, no. 1, 2011, pp. 1–122.
- [22] J. Jiang, C. Han, W. X. Zhao, and J. Wang, “Pdformer: Propagation delay-aware dynamic long-range transformer for traffic flow prediction,” in *Proceedings of the AAAI conference on artificial intelligence*, vol. 37, no. 4, 2023, pp. 4365–4373.
- [23] P.-Y. Chen and S. Liu, “Bias-variance tradeoff of graph Laplacian regularizer,” *IEEE Signal Processing Letters*, vol. 24, no. 8, pp. 1118–1122, 2017.
- [24] T. Hawkins, “Cauchy and the spectral theory of matrices,” *Historia Mathematica*, vol. 2, no. 1, pp. 1–29, 1975. [Online]. Available: <https://www.sciencedirect.com/science/article/pii/0315086075900324>
- [25] S. Chen, A. Sandryhaila, J. Moura, and J. Kovacevic, “Signal recovery on graphs: Variation minimization,” in *IEEE Transactions on Signal Processing*, vol. 63, no. 17, September 2015, pp. 4609–4624.
- [26] Y. Li, H. Vicky Zhao, and G. Cheung, “Eigen-decomposition-free directed graph sampling via Gershgorin disc alignment,” in *ICASSP 2023 - 2023 IEEE International Conference on Acoustics, Speech and Signal Processing (ICASSP)*, 2023, pp. 1–5.
- [27] H. Zou and T. Hastie, “Regularization and Variable Selection Via the Elastic Net,” *Journal of the Royal Statistical Society Series B: Statistical Methodology*, vol. 67, no. 2, pp. 301–320, 03 2005. [Online]. Available: <https://doi.org/10.1111/j.1467-9868.2005.00503.x>
- [28] S. Boyd and L. Vandenberghe, *Convex Optimization*. Cambridge, 2004.
- [29] J. R. Shewchuk, “An introduction to the conjugate gradient method without the agonizing pain,” USA, Tech. Rep., 1994.
- [30] M. Vetterli and J. Kovacevic, “Wavelets and subband coding,” in *Prentice Hall Signal Processing Series*, 2013. [Online]. Available: <https://api.semanticscholar.org/CorpusID:10506924>
- [31] Y. Li, R. Yu, C. Shahabi, and Y. Liu, “Diffusion convolutional recurrent neural network: Data-driven traffic forecasting,” *arXiv preprint arXiv:1707.01926*, 2017.
- [32] S. Guo, Y. Lin, H. Wan, X. Li, and G. Cong, “Learning dynamics and heterogeneity of spatial-temporal graph data for traffic forecasting,” *IEEE Transactions on Knowledge and Data Engineering*, vol. 34, no. 11, pp. 5415–5428, 2022.
- [33] G. C. Reinsel, *Elements of multivariate time series analysis*. Springer Science & Business Media, 2003.
- [34] B. Yu, H. Yin, and Z. Zhu, “Spatio-temporal graph convolutional networks: A deep learning framework for traffic forecasting,” in *Proceedings of the Twenty-Seventh International Joint Conference on Artificial Intelligence*, ser. IJCAI-2018. International Joint Conferences on Artificial Intelligence Organization, Jul. 2018, p. 3634–3640. [Online]. Available: <http://dx.doi.org/10.24963/ijcai.2018/505>

- [35] “Spatial-temporal synchronous graph convolutional networks: A new framework for spatial-temporal network data forecasting,” vol. 34, pp. 914–921, Apr. 2020. [Online]. Available: <https://ojs.aaai.org/index.php/AAAI/article/view/5438>
- [36] Y. Fang, Y. Qin, H. Luo, F. Zhao, B. Xu, L. Zeng, and C. Wang, “When spatio-temporal meet wavelets: Disentangled traffic forecasting via efficient spectral graph attention networks,” in *2023 IEEE 39th international conference on data engineering (ICDE)*. IEEE, 2023, pp. 517–529.
- [37] H. Liu, Z. Dong, R. Jiang, J. Deng, J. Deng, Q. Chen, and X. Song, “Spatio-temporal adaptive embedding makes vanilla transformer sota for traffic forecasting,” in *Proceedings of the 32nd ACM International Conference on Information and Knowledge Management*, 2023, pp. 4125–4129.
- [38] V. P. Dwivedi and X. Bresson, “A generalization of transformer networks to graphs,” *arXiv preprint arXiv:2012.09699*, 2020.
- [39] A. Vaswani, S. Bengio, E. Brevdo, F. Chollet, A. N. Gomez, S. Gouws, L. Jones, L. Kaiser, N. Kalchbrenner, N. Parmar, R. Sepassi, N. Shazeer, and J. Uszkoreit, “Tensor2tensor for neural machine translation,” *CoRR*, vol. abs/1803.07416, 2018. [Online]. Available: <http://arxiv.org/abs/1803.07416>
- [40] W. Hamilton, Z. Ying, and J. Leskovec, “Inductive representation learning on large graphs,” *Advances in neural information processing systems*, vol. 30, 2017.
- [41] P. Ramachandran, B. Zoph, and Q. V. Le, “Swish: a self-gated activation function,” *arXiv preprint arXiv:1710.05941*, vol. 7, no. 1, p. 5, 2017.

## A Proof of Theorem 3.1

We prove Theorem 3.1 by construction as follows. A directed line graph  $\mathcal{G}^d$  of  $N$  nodes with inter-node edge weights 1 (and self-loop of weight 1 at node 1) has adjacency matrix  $\mathbf{W}_r^d$  and random-walk Laplacian matrix  $\mathbf{L}_r^d = \mathbf{I}_N - \mathbf{W}_r^d$  of the following forms:

$$\mathbf{W}_r^d = \begin{bmatrix} 1 & 0 & \dots & 0 \\ 1 & 0 & \dots & 0 \\ 0 & 1 & 0 & \dots & 0 \\ \vdots & \ddots & \ddots & & 0 \\ 0 & \dots & 0 & 1 & 0 \end{bmatrix}, \quad \mathbf{L}_r^d = \begin{bmatrix} 0 & 0 & \dots & 0 \\ -1 & 1 & \dots & 0 \\ 0 & -1 & 1 & \dots & 0 \\ \vdots & \ddots & \ddots & & 0 \\ 0 & \dots & 0 & -1 & 1 \end{bmatrix}. \quad (23)$$

Note that rows 2 to  $N$  of  $\mathbf{L}_r^d$  actually compose the *incidence* matrix of an undirected line graph  $\mathcal{G}^u$  with edge weights 1. Thus, the symmetrized directed graph Laplacian  $\mathcal{L}_r^d = (\mathbf{L}_r^d)^\top \mathbf{L}_r^d$  is also the combinatorial graph Laplacian  $\mathbf{L}^u$ :

$$\mathcal{L}_r^d = \mathbf{L}^u = \begin{bmatrix} 1 & -1 & 0 & \dots & 0 \\ -1 & 2 & -1 & 0 & \dots & 0 \\ 0 & -1 & 2 & -1 & 0 & \dots & 0 \\ \vdots & & \ddots & \ddots & \ddots & & \\ 0 & \dots & 0 & -1 & 2 & -1 \\ 0 & \dots & & 0 & -1 & 1 \end{bmatrix}. \quad (24)$$

As an illustration, consider a 4-node directed line graph  $\mathcal{G}^d$  with edge weights 1; see Fig. 2(a) for an illustration. We see that the symmetrized directed graph Laplacian  $\mathcal{L}_r^d$  defaults to the graph Laplacian  $\mathbf{L}^u$  for a 4-node *undirected* line graph  $\mathcal{G}^u$  (Fig. 2(b)):

$$\mathbf{W}_r^d = \begin{bmatrix} 1 & 0 & 0 & 0 \\ 1 & 0 & 0 & 0 \\ 0 & 1 & 0 & 0 \\ 0 & 0 & 1 & 0 \end{bmatrix}, \quad \mathbf{L}_r^d = \begin{bmatrix} 0 & 0 & 0 & 0 \\ -1 & 1 & 0 & 0 \\ 0 & -1 & 1 & 0 \\ 0 & 0 & -1 & 1 \end{bmatrix}, \quad \mathcal{L}_r^d = \begin{bmatrix} 1 & -1 & 0 & 0 \\ -1 & 2 & -1 & 0 \\ 0 & -1 & 2 & -1 \\ 0 & 0 & -1 & 1 \end{bmatrix}. \quad (25)$$

## B Interpreting Linear System (10)

For notation simplicity, we first define

$$\mathbf{r}^\tau \triangleq (\mathbf{L}_r^d)^\top \left( \frac{\gamma^\tau}{2} + \frac{\rho}{2} \phi^\tau \right) - \frac{\gamma_u^\tau}{2} + \frac{\rho_u}{2} \mathbf{z}_u^\tau - \frac{\gamma_d^\tau}{2} + \frac{\rho_d}{2} \mathbf{z}_d^\tau. \quad (26)$$

Solution  $\mathbf{x}^{\tau+1}$  to linear system (10) can now be written as

$$\mathbf{x}^{\tau+1} = \left( \mathbf{H}^\top \mathbf{H} + \frac{\rho}{2} \mathcal{L}_r^d + \frac{\rho_u + \rho_d}{2} \mathbf{I} \right)^{-1} (\mathbf{r}^\tau + \mathbf{H}^\top \mathbf{y}). \quad (27)$$

Define  $\tilde{\mathcal{L}}_r^d \triangleq \mathbf{H}^\top \mathbf{H} + \frac{\rho}{2} \mathcal{L}_r^d$ . Note that  $\mathbf{H}^\top \mathbf{H}$  is a diagonal matrix with zeros and ones (corresponding to chosen sample indices) along its diagonal, and thus  $\tilde{\mathcal{L}}_r^d$  is a scaled variant of  $\mathcal{L}_r^d$  with the addition of selected self-loops of weight 1. Given that  $\mathcal{L}_r^d = (\mathbf{L}_r^d)^\top \mathbf{L}_r^d$  is real and symmetric,  $\tilde{\mathcal{L}}_r^d$  is also real and symmetric. By eigen-decomposing  $\tilde{\mathcal{L}}_r^d = \tilde{\mathbf{U}} \text{diag}(\{\tilde{\xi}_k\}) \tilde{\mathbf{U}}^\top$ , we can rewrite  $\mathbf{x}^{\tau+1}$  as

$$\mathbf{x}^{\tau+1} = \tilde{\mathbf{U}} \text{diag} \left( \left\{ \frac{1}{\frac{\rho_u + \rho_d}{2} + \tilde{\xi}_k} \right\} \right) \tilde{\mathbf{U}}^\top (\mathbf{r}^\tau + \mathbf{H}^\top \mathbf{y}) \quad (28)$$

which demonstrates that  $\mathbf{x}^{\tau+1}$  is a low-pass filter output of up-sampled  $\mathbf{H}^\top \mathbf{y}$  (with bias  $\mathbf{r}^\tau$ ).

## C Deriving Solution to Optimization (15)

The optimization for  $\phi$  in objective (15) can be performed entry-by-entry. Specifically, for the  $i$ -th entry  $\phi_i$ :

$$\min_{\phi_i} g(\phi_i) = \mu_{d,1} |\phi_i| + \gamma_i^\tau (\phi_i - (\mathbf{L}_r^d)_i \mathbf{x}^{\tau+1}) + \frac{\rho}{2} (\phi_i - (\mathbf{L}_r^d)_i \mathbf{x}^{\tau+1})^2 \quad (29)$$

where  $(\mathbf{L}_r^d)_i$  denotes the  $i$ -row of  $\mathbf{L}_r^d$ .  $g(\phi_i)$  is convex and differentiable when  $\phi_i \neq 0$ . Specifically, when  $\phi_i > 0$ , setting the derivative of  $g(\phi_i)$  w.r.t.  $\phi_i$  to zero gives

$$\begin{aligned} \mu_{d,1} + \gamma_i^\tau + \rho (\phi_i^* - (\mathbf{L}_r^d)_i \mathbf{x}^{\tau+1}) &= 0 \\ \phi_i^* &= (\mathbf{L}_r^d)_i \mathbf{x}^{\tau+1} - \rho^{-1} \gamma_i^\tau - \rho^{-1} \mu_{d,1} \end{aligned} \quad (30)$$

which holds only if  $(\mathbf{L}_r^d)_i \mathbf{x}^{\tau+1} - \rho^{-1} \gamma_i^\tau > \rho^{-1} \mu_{d,1}$ . On the other hand, when  $\phi_i < 0$ ,

$$\begin{aligned} -\mu_{d,1} + \gamma_i^\tau + \rho (\phi_i^* - (\mathbf{L}_r^d)_i \mathbf{x}^{\tau+1}) &= 0 \\ \phi_i^* &= (\mathbf{L}_r^d)_i \mathbf{x}^{\tau+1} - \rho^{-1} \gamma_i^\tau + \rho^{-1} \mu_{d,1} \end{aligned} \quad (31)$$

which holds only if  $(\mathbf{L}_r^d)_i \mathbf{x}^{\tau+1} - \rho^{-1} \gamma_i^\tau < -\rho^{-1} \mu_{d,1}$ . Summarizing the two cases, we get

$$\begin{aligned} \delta &= (\mathbf{L}_r^d)_i \mathbf{x}^{\tau+1} - \rho^{-1} \gamma_i^\tau \\ \phi_i^* &= \text{sign}(\delta) \cdot \max(|\delta| - \rho^{-1} \mu_{d,1}, 0) \end{aligned} \quad (32)$$

**Alternative solution with subgradients:** Denote  $g_1(\phi) = \mu_{d,1} \|\phi\|_1$ ,  $g_2(\phi) = (\gamma^\tau)^\top (\phi - \mathbf{L}_r^d \mathbf{x}^{\tau+1}) + \frac{\rho}{2} \|\phi - \mathbf{L}_r^d \mathbf{x}^{\tau+1}\|_2^2$ , the subgradient of  $g(\phi)$  is

$$\partial g(\phi) = \{\mathbf{g} + \nabla g_2(\phi) | \mathbf{g} \in \partial g_1(\phi)\} = \{\mu_{d,1} \sigma + \gamma^\tau + \rho(\phi - \mathbf{L}_r^d \mathbf{x}^{\tau+1}) | \sigma \in \partial(\|\phi\|_1)\}, \quad (33)$$

where

$$\partial_i(\|\phi\|_1) = \begin{cases} \text{sign}(\phi_i), & \phi_i \neq 0, \\ [-1, 1], & \phi_i = 0. \end{cases} \quad (34)$$

The minimal  $\phi^*$  satisfies  $\mathbf{0} \in \partial g(\phi^*)$ , thus

$$\begin{aligned} \mu_{d,1} + \gamma_i^\tau + \rho(\phi_i^* - (\mathbf{L}_r^d)_i \mathbf{x}) &= 0, & \text{if } \phi_i^* > 0, \\ -\mu_{d,1} + \gamma_i^\tau + \rho(\phi_i^* - (\mathbf{L}_r^d)_i \mathbf{x}) &= 0, & \text{if } \phi_i^* < 0, \\ \exists \sigma \in [-1, 1], \text{ s.t. } \mu_{d,1}\sigma + \gamma_i^\tau + \rho(\phi_i^* - (\mathbf{L}_r^d)_i \mathbf{x}) &= 0, & \text{if } \phi_i^* = 0, \end{aligned} \quad (35)$$

which gives

$$\phi_i^* = \begin{cases} (\mathbf{L}_r^d)_i \mathbf{x} - \frac{\gamma_i^\tau}{\rho} - \frac{\mu_{d,1}}{\rho}, & (\mathbf{L}_r^d)_i \mathbf{x} - \frac{\gamma_i^\tau}{\rho} > \frac{\mu_{d,1}}{\rho} \\ 0, & -\frac{\mu_{d,1}}{\rho} \leq (\mathbf{L}_r^d)_i \mathbf{x} - \frac{\gamma_i^\tau}{\rho} \leq \frac{\mu_{d,1}}{\rho} \\ (\mathbf{L}_r^d)_i \mathbf{x} - \frac{\gamma_i^\tau}{\rho} + \frac{\mu_{d,1}}{\rho}, & (\mathbf{L}_r^d)_i \mathbf{x} - \frac{\gamma_i^\tau}{\rho} < -\frac{\mu_{d,1}}{\rho} \end{cases}. \quad (36)$$

Thus the solution of (15) is

$$\phi^{\tau+1} = \phi^* = \text{soft}_{\frac{\mu_{d,1}}{\rho}} \left( \mathbf{L}_r^d \mathbf{x} - \frac{\gamma_i^\tau}{\rho} \right) = \text{sign} \left( \mathbf{L}_r^d \mathbf{x} - \frac{\gamma_i^\tau}{\rho} \right) \max \left( \left| \mathbf{L}_r^d \mathbf{x} - \frac{\gamma_i^\tau}{\rho} \right| - \frac{\mu_{d,1}}{\rho}, 0 \right). \quad (37)$$

## D Parameterizing Conjugated Gradient Method in Solving Linear Equations

A linear system  $\mathbf{A}\mathbf{x} = \mathbf{b}$  where  $\mathbf{A}$  is a PD matrix can be solved iteratively by the conjugated gradient (CG) method, as is described in Algorithm 1. We parameterize the coefficients of the ‘‘gradients’’  $\alpha_k$  and ‘‘momentum’’  $\beta_k$  in each CG iteration to transform the iterative algorithm to stacked neural net layers. Note that  $\alpha, \beta \geq 0$  in every iteration in the original algorithm, and should be kept non-negative in the unrolled version.

---

### Algorithm 1 Conjugate Gradient (CG) Method to Solve $\mathbf{A}\mathbf{x} = \mathbf{b}$

---

**Require:** PSD matrix  $\mathbf{A} \in \mathbb{R}^{n \times n}$ , vector  $\mathbf{b} \in \mathbb{R}^n$ , initial guess  $\mathbf{x}_0$

**Ensure:** Approximate solution  $\mathbf{x}$  such that  $\|\mathbf{A}\mathbf{x} - \mathbf{b}\| \leq \epsilon$ , where  $\epsilon$  is the tolerance of convergence

```

1:  $\mathbf{r}_0 \leftarrow \mathbf{b} - \mathbf{A}\mathbf{x}_0$  ▷ Initial residual
2:  $\mathbf{p}_0 \leftarrow \mathbf{r}_0$ 
3:  $k \leftarrow 0$ 
4: while  $\|\mathbf{A}\mathbf{x}_k - \mathbf{b}\| > \epsilon$  do
5:    $\alpha_k \leftarrow \frac{\mathbf{r}_k^\top \mathbf{r}_k}{\mathbf{p}_k^\top \mathbf{A} \mathbf{p}_k}$ 
6:    $\mathbf{x}_{k+1} \leftarrow \mathbf{x}_k + \alpha_k \mathbf{p}_k$ 
7:    $\mathbf{r}_{k+1} \leftarrow \mathbf{r}_k - \alpha_k \mathbf{A} \mathbf{p}_k$  ▷ Dual residual
8:    $\beta_k \leftarrow \frac{\mathbf{r}_{k+1}^\top \mathbf{r}_{k+1}}{\mathbf{r}_k^\top \mathbf{r}_k}$ 
9:    $\mathbf{p}_{k+1} \leftarrow \mathbf{r}_{k+1} + \beta_k \mathbf{p}_k$ 
10:   $k \leftarrow k + 1$ 
11: end while
12: return  $\mathbf{x}_{k+1}$ 

```

---

## E Model Setup

### E.1 ADMM Blocks Setup

We initialize  $\mu_u, \mu_{d,1}, \mu_{d,2}$  with 3, and the  $\rho, \rho_u, \rho_d$  with  $\sqrt{N/(T+S+1)}$ , where  $N$  is the number of sensors and  $T+S+1$  is the full length of the recovered signal (both the observed part and the part to be predicted). Those parameters are trained every ADMM layer. We initialize the CGD parameters  $(\alpha, \beta)$ s as 0.08, and tune them for every CGD iteration. We clamp each element of the CGD step size  $\alpha$  to  $[0, 0.8]$  for stability. Each element of the momentum term coefficient  $\beta$  is clamped to be non-negative.

## E.2 Graph Learning Modules Setup

We define multiple PD matrices  $\mathbf{P}$ s and  $\mathbf{M}$ s in our unrolling model due to the different impact strengths at different times. For the undirected graph, we define  $\mathbf{M}^t$  as the Mahanabolis distance matrix for the undirected graph slice at time  $t$  to vary the impacting strength between spatial neighbors in different time steps. For the directed graph, we assume that the impact strength varies with different *intervals* but remains uniform for different monitoring stations. Thus, we define  $\mathbf{P}^w$  as the Mahanabolis distance matrix to represent the temporal influence of interval  $w$  for each node. Therefore, we define  $(T + S + 1)$  learnable PSD matrices  $\mathbf{M}^0, \dots, \mathbf{M}^{T+S}$  for undirected graph learning, and  $W$  PSD learnable matrices  $\mathbf{P}^1, \dots, \mathbf{P}^W$  for directed graph learning in total.

We learn each PSD matrix  $\mathbf{M}$  in each UGL by learning a square matrix  $\mathbf{M}_0 \in \mathbb{R}^{K \times K}$  by  $\mathbf{M} = \mathbf{M}_0^\top \mathbf{M}_0$ , and initialize  $\mathbf{M}_0$  with a matrix whose diagonal is filled with 1.5. Similarly, we learn each PSD matrix  $\mathbf{P}^w$  in DGL by learning  $\mathbf{P}_0^w$  where  $\mathbf{P}^w = (\mathbf{P}_0^w)^\top \mathbf{P}_0^w$ . We initialize  $\mathbf{P}_0^w$  with  $(1 + 0.2w/W)\mathbf{I}$  to set the edge weights representing influences of longer intervals slightly smaller.

We learn 4 mixed graphs in parallel with 4 sets of matrices  $\mathbf{M}^0, \dots, \mathbf{M}^{T+S}$  and  $\mathbf{P}^1, \dots, \mathbf{P}^W$  to implement the *multi-head* attention mechanism in conventional transformers. The output signals of all 4 channels are integrated to one by a linear layer at the end of each ADMM block.

## E.3 Feature Extractors Setup

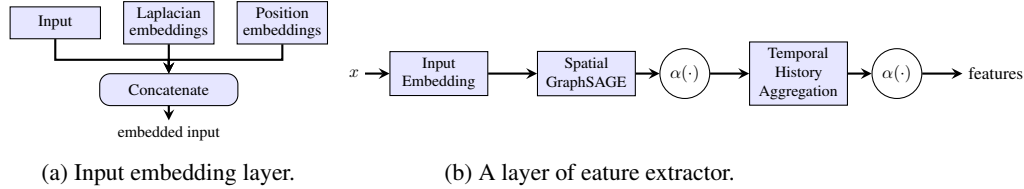


Figure 4: Framework of our feature extractor. (a) We first propose a non-parametric input embedding layer to combine signal with spatial/temporal embeddings. (b) Then aggregate embedded inputs of spatial neighbors and history information in a time window to generate a layer of feature extractor.

We detailedly introduce our design of the feature extractor described in Section 4.3. Figure 4b shows the overall structure of our feature extractors.

### E.3.1 Input Embeddings

We generate *non-parametric* spatial and temporal embeddings for each node in our mixed spatio-temporal graph, see Figure 4a. For spatial embeddings, we first generate the adjacency matrix  $\mathbf{W}^s$  for the real-world connection of monitor stations using the physical distances  $d^s(i, j)$  with

$$w_{i,j}^s = w_{j,i}^s = \exp \left[ -\frac{(d^s(i, j))^2}{50 \times \text{Var}(d^s)} \right], \quad (38)$$

where  $\text{Var}(d^s)$  denotes the variance of the physical distances. We use Laplacian embedding supposed by Dwivedi and Bresson [38], which uses the eigenvectors of the  $k^s$ -smallest non-zero eigenvalues of the Laplacian matrix  $\mathbf{L}^s = \mathbf{D}^s - \mathbf{W}^s$  to generate  $k$ -dimensional embeddings. Our experiments set  $k^s = 5$ .

For temporal embeddings, we use the sine-cosine position embeddings[39]:

$$\begin{aligned} e[t, 2i] &= \sin(t/10000^i) \\ e[t, 2i + 1] &= \cos(t/10000^i), i = 0, 1, \dots, \left\lfloor \frac{k^T}{2} \right\rfloor - 1. \end{aligned} \quad (39)$$

We follow Feng and Tassiulas [9] to use real-time-stamp, time-in-day and day-in-week embeddings of dimensions 10, 6, 4.

We directly concatenate these spatial and temporal embedding to our signals  $\mathbf{x}_j^t$  for node  $j$  at time  $t$  as  $\mathbf{e}_j^t = [\mathbf{x}_j^t; \mathbf{e}_j^S; \mathbf{e}_t^T]$  for feature extractors, where  $\mathbf{e}_j^S$  denote the spatial Laplacian embeddings of node  $j$  of the physical graph, and  $\mathbf{e}_t^T$  denotes the temporal position embeddings of time step  $t$ .

### E.3.2 Feature Extraction from embeddings

We use a variant of GraphSAGE [40] to aggregate spatial features and introduce Temporal History Aggregation (THA) to aggregate temporal features. The GraphSAGE module aggregates the inputs of each node’s  $k$ -NNs with a simple and uniform linear layer to generate  $K$ -dimension spatial features for each node of each time step. The THA module aggregates the embedded inputs of past  $W$  time steps for each node with a uniform linear layer, where  $W$  is the size of the time window. For both GraphSAGE and THA modules, we pad zeros to inputs as placeholders, and use Swish [41] as activation functions with  $\beta = 0.8$ .

### E.4 Constructing Graphs $\mathbf{W}^{u,0}$ , $\mathbf{W}^{d,0}$ for the First ADMM Block

Our ADMM block recovers the full signal  $\mathbf{x}$  from observed signal  $\mathbf{y}$  with mixed graph  $\mathcal{G}^u, \mathcal{G}^d$  constructed from embedded *full* signal  $\mathbf{e} = [\mathbf{x}; \mathbf{e}^S; \mathbf{e}^T]$ . Thus, for the first block in ADMM, we need an *initial extrapolation* for the signals to predict.

We propose a simple module to make an initial guess of the signals: we modify the feature extractor described in Appendix E.3.2 to generate intermediate features from the embedded input of the observed part. Then we combine the feature and temporal dimensions, and use a simple linear layer with Swish activation to generate the initially extrapolated signal.

**Note:** Both the feature extractor and the initial prediction module are carefully designed to involve as few parameters as possible to make the entire model lightweight. Furthermore, low-parameter and simple feature engineering ensures that the effectiveness of our model is attributed to the unrolled blocks and graph learning modules, rather than to the trivial feature engineering parts.

### E.5 Training Setup

We preprocess the dataset by *standardizing* the entire time series for each node in space, but minimize a loss between the real groundtruth signal and the *rescaled* whole output signal. We use an Adam optimizer with learning rate  $5 \times 10^{-4}$ , together with a scheduler of reduction on validation loss with a reduction rate of 0.2 and patience of 5. We set different batch sizes for different datasets to leverage the most of the GPU memory (in this case, we use an entire Nvidia GeForce RTX 3090). Detailed selection of parameters such as number of nearest spatial neighbors  $k$  and time window size  $W$  is shown in Table 4.

Table 4: Training setup of graph construction and batch size for all traffic datasets.

Dataset	PeMS03	PeMS04	METR-LA	PEMS-BAY
$k$	4	6	6	6
$W$	6	6	6	4
Batch size	12	12	16	12

## F Optimization Formulation and ADMM Algorithm in Ablation Studies

### F.1 Optimization & Algorithm without DGTV Term

By removing the DGTV term  $\|\mathbf{L}_r^d \mathbf{x}\|_1$  in (4), and introducing the auxiliary variables  $\mathbf{z}_u, \mathbf{z}_d$  as (9), we rewrite the unconstrained version of the optimization by augmented Lagrangian method as

$$\begin{aligned}
\min_{\mathbf{x}, \mathbf{z}_u, \mathbf{z}_d} & \|\mathbf{y} - \mathbf{H}\mathbf{x}\|_2^2 + \mu_u \mathbf{z}_u^\top \mathbf{L}^u \mathbf{z}_u + \mu_{d,2} \mathbf{z}_d^\top \mathcal{L}_r^d \mathbf{z}_d + (\gamma_u^\tau)^\top (\mathbf{x} - \mathbf{z}_u) + \frac{\rho_u}{2} \|\mathbf{x} - \mathbf{z}_u\|_2^2 \\
& + (\gamma_d^\tau)^\top (\mathbf{x} - \mathbf{z}_d) + \frac{\rho_d}{2} \|\mathbf{x} - \mathbf{z}_d\|_2^2.
\end{aligned} \tag{40}$$



We optimize  $\mathbf{x}$ ,  $\mathbf{z}_u$  and  $\mathbf{z}_d$  in turn at iteration  $\tau$  as follows:

$$\left(\mathbf{H}^\top \mathbf{H} + \frac{\rho_u + \rho_d}{2} \mathbf{I}\right) \mathbf{x}^{\tau+1} = \mathbf{H}^\top \mathbf{y} - \frac{\gamma_u^\tau + \gamma_d^\tau}{2} + \frac{\rho_u}{2} \mathbf{z}_u^\tau + \frac{\rho_d}{2} \mathbf{z}_d^\tau, \quad (41)$$

$$\left(\mu_u \mathbf{L}^u + \frac{\rho_u}{2} \mathbf{I}\right) \mathbf{z}_u^{\tau+1} = \frac{\gamma_u^\tau}{2} + \frac{\rho_u}{2} \mathbf{x}^{\tau+1}, \quad (42)$$

$$\left(\mu_d \mathcal{L}_r^d + \frac{\rho_d}{2} \mathbf{I}\right) \mathbf{z}_d^{\tau+1} = \frac{\gamma_d^\tau}{2} + \frac{\rho_d}{2} \mathbf{x}^{\tau+1}. \quad (43)$$

The updating of  $\gamma_u^\tau, \gamma_d^\tau$  follows (18).

## F.2 Optimization & Algorithm without DGLR Term

By removing the DGLR term  $\mathbf{x} \mathcal{L}_r^d \mathbf{x}$  in (4) and introduce only the auxiliary variables  $\phi$  in (5) and  $\mathbf{z}_u$  in (9), we rewrite the unconstrained version of the optimization of  $\mathbf{x}^{\tau+1}$  by augmented Lagrangian method as

$$\min_{\mathbf{x}, \mathbf{z}_u} \|\mathbf{y} - \mathbf{H}\mathbf{x}\|_2^2 + \mu_u \mathbf{z}_u^\top \mathbf{L}^u \mathbf{z}_u + (\gamma^\tau)^\top (\phi^\tau - \mathbf{L}_r^d \mathbf{x}) + \frac{\rho}{2} \|\phi^\tau - \mathbf{L}_r^d \mathbf{x}\|_2^2 + (\gamma_u^\tau)^\top (\mathbf{x} - \mathbf{z}_u) + \frac{\rho_u}{2} \|\mathbf{x} - \mathbf{z}_u\|_2^2 \quad (44)$$

We optimize  $\mathbf{x}$  and  $\mathbf{z}_u$  in turn at iteration  $\tau$  as follows:

$$\left(\mathbf{H}^\top \mathbf{H} + \frac{\rho}{2} \mathcal{L}_r^d + \frac{\rho_u}{2} \mathbf{I}\right) \mathbf{x}^{\tau+1} = \mathbf{H}^\top \mathbf{y} + (\mathbf{L}_r^d)^\top \left(\frac{\gamma^\tau}{2} + \frac{\rho}{2} \phi^\tau\right) - \frac{\gamma_u^\tau}{2} + \frac{\rho_u}{2} \mathbf{z}_u^\tau \quad (45)$$

$$\left(\mu_u \mathbf{L}^u + \frac{\rho_u}{2} \mathbf{I}\right) \mathbf{z}_u^{\tau+1} = \frac{\gamma_u^\tau}{2} + \frac{\rho_u}{2} \mathbf{x}^{\tau+1} \quad (46)$$

The optimization of  $\phi^{\tau+1}$  is the same as (15), and the solution is the same as (16). The updating of  $\gamma, \gamma_u$  follows (17) and (18).

## F.3 Algorithm Unrolling with an Undirected Temporal Graph

In this section, we are changing the directed temporal graph  $\mathcal{G}^d$  into an *undirected* graph while maintaining the connections. Denote the undirected temporal graph as  $\mathcal{G}^n$ . We introduce the GLR operator  $\mathbf{x}^\top \mathbf{L}^n \mathbf{x}$  for  $\mathcal{G}^n$  on signal  $\mathbf{x}$  where  $\mathbf{L}^n$  is the normalized Laplacian matrix of  $\mathcal{G}^n$ . Thus the optimization problem is as follows:

$$\min_{\mathbf{x}} \|\mathbf{y} - \mathbf{H}\mathbf{x}\|_2^2 + \mu_u \mathbf{x}^\top \mathbf{L}^u \mathbf{x} + \mu_n \mathbf{x}^\top \mathbf{L}^n \mathbf{x} \quad (47)$$

where  $\mu_u, \mu_n \in \mathbb{R}_+$  are weight parameters for the two GLR priors. The optimization is similar to that in Appendix F.1. By a similar approach which introduces auxiliary variables  $\mathbf{z}_u = \mathbf{x}, \mathbf{z}_n = \mathbf{x}$ , we optimize  $\mathbf{x}, \mathbf{z}_u, \mathbf{z}_n$  as follows:

$$\left(\mathbf{H}^\top \mathbf{H} + \frac{\rho_u + \rho_n}{2} \mathbf{I}\right) \mathbf{x}^{\tau+1} = \mathbf{H}^\top \mathbf{y} - \frac{\gamma_u^\tau + \gamma_n^\tau}{2} + \frac{\rho_u}{2} \mathbf{z}_u^\tau + \frac{\rho_n}{2} \mathbf{z}_n^\tau, \quad (48)$$

$$\left(\mu_u \mathbf{L}^u + \frac{\rho_u}{2} \mathbf{I}\right) \mathbf{z}_u^{\tau+1} = \frac{\gamma_u^\tau}{2} + \frac{\rho_u}{2} \mathbf{x}^{\tau+1}, \quad (49)$$

$$\left(\mu_n \mathbf{L}^n + \frac{\rho_n}{2} \mathbf{I}\right) \mathbf{z}_n^{\tau+1} = \frac{\gamma_n^\tau}{2} + \frac{\rho_n}{2} \mathbf{x}^{\tau+1}. \quad (50)$$

The updating of  $\gamma_u^\tau, \gamma_n^\tau$  is also similar to (18) as follows:

$$\gamma_u^{\tau+1} = \gamma_u^\tau + \rho_u (\mathbf{x}^{\tau+1} - \mathbf{z}_u^{\tau+1}), \quad \gamma_n^{\tau+1} = \gamma_n^\tau + \rho_n (\mathbf{x}^{\tau+1} - \mathbf{z}_n^{\tau+1}). \quad (51)$$

The undirected temporal graph  $\mathcal{G}^n$  is learned by an UGL described in Section 4.3, and is initialized similar to the spatial UGL described in Appendix E.2. The initialization of  $\mu_n, \rho_n$  and the CGD parameters in solving (50) follows the setup in Appendix E.1.

## G Further Ablation Studies

### G.1 Sensitivity of $k, W$ in Graph Construction

We change the number of spatial nearest neighbors  $k = 4, 6, 8$  and time window size  $W = 4, 6, 8$  and present the results for PEMS03 and METR-LA dataset in Table 5. The selected hyperparameters

are marked with “\*”. Decreasing or increasing  $k, W$  leads to performance degradation. Our selection of  $k, W$  are optimal among all test hyperparameters, considering the tradeoff with the cost of time and memory.

Table 5: Performance on 60-minute forecasting with PEMS03 (left) and METR-LA (right) under different  $k, W$  settings.

PEMS03, 60-minute forecast					METR-LA, 60-minute forecast				
$k$	$W$	RMSE	MAE	MAPE(%)	$k$	$W$	RMSE	MAE	MAPE(%)
4*	6*	27.67	17.46	<b>17.72</b>	6*	6*	<b>12.37</b>	5.27	<b>11.91</b>
4	4	29.54	<b>17.09</b>	17.92	4	6	12.43	<b>5.24</b>	11.87
4	8	<b>27.45</b>	17.25	18.35	8	6	12.61	5.30	11.92
6	6	28.98	17.33	18.23	6	4	12.44	5.40	11.85
8	6	45.37	18.15	20.59	6	8	12.44	5.3525	11.96

## G.2 Sensitivity of Number of Blocks and Layers in the Unrolling Model

We vary the number of blocks and ADMM layers for PEMS03 dataset and present the results in Table 6. The results show that reducing number of blocks or layers will increase the error in prediction. Our selected settings  $n_{\text{blocks}} = 5, n_{\text{layers}} = 25$  is the optimal setting so far in consideration of the trade-off in computing memory and time cost.

Table 6: Performance on 60-minute forecast with PEMS03 dataset under different number of blocks and layers.

$n_{\text{blocks}}$	$n_{\text{layers}}$	PEMS03, 60-minute forecast			METR-LA, 60-minute forecast		
		RMSE	MAE	MAPE(%)	RMSE	MAE	MAPE(%)
5*	25*	<b>27.67</b>	17.46	<b>17.72</b>	<b>12.37</b>	<b>5.27</b>	<b>11.91</b>
5	20	27.95	<b>17.32</b>	18.02	12.53	5.35	12.15
4	25	27.77	17.63	18.61	12.45	5.33	12.00

## G.3 Ablation Study for the Splitting- $\ell_2$ -term Strategy

We also ran ablations of the splitting-term strategy by optimizing  $\mathbf{x}^{\tau+1}$  using only (7). CG in solving (7) converges much slower than in solving (10)-(12), and the unrolled model can become numerically unstable in training, indicating that splitting the  $\ell_2$  terms can stabilize the training process.

## H Error Bar for Our Model in Table 1

Table 7 shows the  $2\sigma$  error bars of our model’s performance in the 60-minute forecast in Table 1 in Section 5, each of which is computed from 3 runs on different random seeds.

Table 7:  $2\sigma$  error bar of the performance metrics of our model in 60-minute traffic forecast in all three datasets.

Dataset	PeMS03	METR-LA	PEMS-BAY
$2\sigma_{\text{RMSE}}$	0.05	0.04	0.01
$2\sigma_{\text{MAE}}$	0.02	0.02	0.01
$2\sigma_{\text{MAPE}(%)}$	0.03	0.04	0.10

## I Reconstruction Error

We perform the spatial/temporal forecast by recovering the *entire* time-vertex signal, which is unusual compared to other deep models. Table 8 shows that the reconstruction error is much smaller than

the predicted part, indicating that our model has extracted all spatial/temporal correlations from the observed part for prediction.

Table 8: Reconstruction RMSE for the observed signals in 60-minute forecast in all three datasets.

<b>Dataset</b>	PEMS03	METR-LA	PEMS-BAY
<b>rec RMSE</b>	1.44	0.49	0.39